Mechatronics 57 (2019) 173–187

Contents lists available at ScienceDirect

Mechatronics

journal homepage: www.elsevier.com/locate/mechatronics

A unified framework for operational range estimation of mobile robots operating on a single discharge to avoid complete immobilization☆

Kshitij Tiwari[a,d,1,*], Xuesu Xiao[b], Ashish Malik[c], Nak Young Chong[d]

[a] School of Electrical Engineering, Aalto University, Espoo, 02150, Finland
[b] Department of Computer Science & Engineering, Texas A&M University, College Station, Texas, 77843, United States
[c] Department of Mechanical Engineering, PEC University of Tech., Chandigarh, 160012, India
[d] School of Information Science, Japan Adv. Inst. of Sc. & Tech. (JAIST), Ishikawa, 923–1292, Japan

A B S T R A C T

Mobile robots are being increasingly deployed in fields where human intervention is deemed risky. However, in doing so, one of the prime concern is to prevent complete battery depletion which may in turn lead to immobilization of the robot during the mission. Thus, we need to carefully manage the energy available to explore as much of the unknown environment as feasible whilst guaranteeing a safe return journey to home base. For this, we need to identify the key components that draw energy and quantify their individual energy requirements. However, this problem is difficult due to the fact that most of the robots have different motion models, and the energy consumption usually also varies from mission to mission. It is desirable to have a generic framework that takes into account different locomotion models and possible mission profiles. This paper presents a methodology to unify the energy consumption models for various robotic platforms thereby allowing us to estimate operational range in both offline and online fashions. The existing models consider a given mission profile and try to estimate its energy requirements whilst our model considers the energy as a given resource constraint and tries to optimize the mission to be accomplished within these constraints. The proposed unified energy consumption framework is verified by field experiments for micro UGV and multi-rotor UAV test-beds operating under myriad of environmental conditions. The *online* model estimates operational range with an average accuracy (measured with respect to true range across multiple field trials) of 93.87% while the *offline* model attains 82.97%.

1. Introduction

Most of the commercially available robots and other experimental platforms widely used for field experiments are powered by a portable battery. Thus, the capacity of the battery affects the overall mission duration and performance. Most of the times, the robots are used in DDD (Dangerous, Dirty, and Dull) environments [25]. This applies to most kinds of mobile robot platforms, including Unmanned Ground Vehicle (UGV), Unmanned Aerial Vehicle (UAV), and Unmanned Marine Vehicle (UMV) as shown in Fig. 1. In such scenarios, if the robot battery is completely depleted, then, the robot will be stranded and must be retrieved either by a human operator thereby increasing life risk or by another robot which increases the project cost. To prevent such scenarios, it is necessary to carefully estimate the energy requirements of a mission and plan the journey such that the exploration is informative[2] and the robot always returns to base station. In order to do so, it is necessary to exhaustively study the energy breakdown of various components of a mobile robot and to quantify them such that energy consumption can be optimized to allow the robots to explore larger proportions of the fields.

Currently, the researchers have proposed either human-controlled strategies, whereby, based on the current battery levels, the human decides when to terminate the mission [28] or a more autonomous extension [7] where the robot can autonomously return to base station to recharge. However, when we deal with DDD environments, recharging or replenishing of power sources is usually deemed infeasible due to time critical nature of the missions. Thus, we need mission planning strategies which can optimize the robot trajectories to simultaneously ensure safe return to base and accrue as much information about the unknown environment as feasible, whilst operating on a single discharge cycle.

This paper serves as an extension of our preliminary findings [32]. In our prior work, we focused on autonomous ground robots operating in approximately smooth terrains with constant change of gradient but now we extend and generalize our previous model to various robotic platforms operating in natural environmental conditions. Before we do

☆ This paper was recommended for publication by Associate Editor Kaddour Bouazza-Marouf

* Corresponding author at: School of Electrical Engineering, Aalto University, Espoo, 02150, Finland
E-mail addresses: kshitij.tiwari@aalto.fi (K. Tiwari), xiaoxuesu@tamu.edu (X. Xiao), ashishmalik.bemech14@pec.edu.in (A. Malik), nakyoung@jaist.ac.jp (N.Y. Chong).

[1] At the time of submission, K. Tiwari was with the School of Information Science, Japan Adv. Inst. of Sc. & Tech. (JAIST), Ishikawa, 923–1292, Japan where the majority of this work was carried out, as a part of his Ph.D.

[2] "informativeness" of exploration could be determined based on user-defined criteria like entropy minimization, maximal area coverage etc.

https://doi.org/10.1016/j.mechatronics.2018.12.006
Received 16 October 2017; Received in revised form 26 October 2018; Accepted 15 December 2018
Available online 29 December 2018
0957-4158/

(a) (b) (c)

Fig. 1. Scenario. Given the nature of the robot. (a) shows a unmanned ground vehicle being utilized to detected land mines in Lebanon (Mine detector robot tested in lebanon field. https://www.youtube.com/watch?v=q78X71nzUZM; 2011); (b) shows an unmanned aerial vehicle being used for forest fire monitoring (Thermalcapture in forest fire management. http://thermalcapture.com/thermalcapture-in-forest-fire-management/; 2018); (c) shows an unmanned marine vehicle that can be used to monitor marine life and pollution (Unmanned marine vehicle. https://tinyurl.com/y785nk4k; 2017). It should be able to estimate its maximal operational range within which the exploration must be completed including the return trip to base.

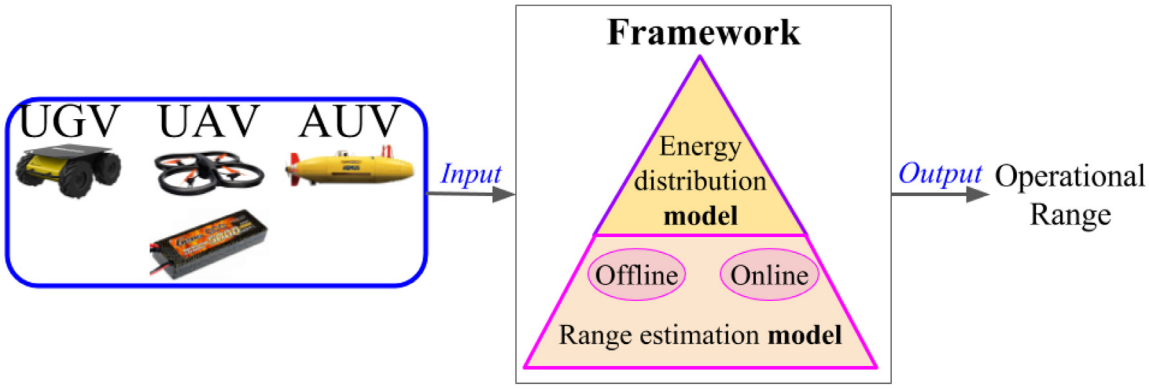

Fig. 2. Framework versus model. Illustrating the difference between the terms "framework" and "model". The term "framework" refers to the overall architecture which houses 2 sub-modules for categorizing energy distribution from battery and models for transforming energy into attainable operational range. On a high level, this architecture is common to all kinds of robots with the difference only in locomotion models which appears in low level of the *online/offline* modules and hence the notion of *unification* is captured.

so, we distinguish between the terms "framework" and "model" aided by Fig. 2. In light of this setting, the generalized framework is no longer restricted by the assumption of wheeled ground locomotion, but is now able to account for different locomotion principles from other regimes and is equally applicable to commercially available or custom built robots. As case studies, we provide detailed explanation as to how our framework can be applied to micro-UGVs and multi-rotor UAVs. To this end, we propose an *offline* variant which relies on expertise of the operator to set an appropriate prior and also an *online* model which determines the model parameters based on real-time operation data. Under this setting, we intend on addressing the following research question: *Given the dynamics model, minimal prior information about operational environment and battery characteristics, how accurately can we estimate the maximal operational range to avoid complete immobilization amidst the mission?*

The rest of the paper is organized as follows: We begin by summarizing some of the state-of-art works related to our work in Section 2 and highlight their limitations which serve as a motivation for our framework. We then explain our proposed framework in Section 3 which is backed by empirical validation shown in Section 4. We conclude this work in Section 5 and propose some future extensions to our proposed framework. All notations have been summarized in Table 1 for the ease of the readers.

2. Related works

The body of work regarding a general robotic energy model is relatively small. Most of the works are purely focused on quantifying / minimizing the energy used only for robot's locomotion and the range estimation is mostly based on real-time energy requirements or learning techniques. In [9], the researchers were concerned about assessing the energy usage of a mobile robot where the robot itself was considered as a "black box". This is not always desirable since the robotic components' energy consumption is of importance as well. Also, pre-defined trajectories were considered to estimate the velocity profile. This is useful to test the model for agile motion as the robot maneuvers along straight stretches and executes turning. But this neither takes into account the impact from variable velocity nor does a robot follow fixed trajectories in real missions. The authors in [29] aimed at predicting the expected mission energy required while a mission is being executed and proposed machine learning techniques for online update of these estimates based on real-time data gathered. Learning techniques may be useful in practice, but the "black box" methodology of neural networks or similar machine learning models provides limited understanding of energy distribution. Since most robots only use one shared battery for all on-board energy consuming components, we need to understand the energy dis-

Table 1
Nomenclature.

Symbol	Description
m_R	Mass of robot
$g = 9.8$	Gravitational acceleration (m/s^2)
C_{rr}	Ground (Rolling) resistance
C_D	Zero drag coefficient
k	Power/data rate coefficient
k_{Env}	Flight adjustment coefficient
k_{Terr}	Terrain variation coefficient
k_r	Propeller constant relating T with ω
$\rho = 1.2041$	Density of air kg/m^3 [1]
A	true area over which drag force is acting (m^2)
θ	terrain elevation (degrees)
d	travel distance (m)
d_{Max}	Max distance (m)
η	Energy loss (%)
$\Gamma = 0.27$	Figure of Merit for UAV propellers [1]
${}^r\Omega_{Man}$	Net maneuvering efficiency of robot r(%)
v	Forward velocity of robot (m/s)
ω	Angular velocity of robot (rad/s)
v_{Opt}	Optimal velocity which allows the robot to attain d_{Max}
k_1, k_2	Positive battery decay coefficients
P_{Man}	Power used by maneuvering branch (W)
P_{Anc}	Power used by ancillary branch (W)
s_0, s_1	Positive sensing coefficients (W)
P_C	Power needed for computation & wireless communication (W)
T	Thrust (N)
τ_D	Drag torque (N-m)
N_R	Number of rotors
r_p	Radius of propellers (m)
$D \triangleq 100 \times \left(\frac{T_M - T_A}{T_M}\right)$	Duty Cycle (% Driving Time) during which maneuvering energy is non-zero
E	Energy available from the battery source (J)
ME	Energy available for maneuvering functions (J)
AE	Energy available for ancillary functions (J)
$Maneuvering$	Tasks involved in navigation like steering, height adjustment etc.
$Ancillary$	Tasks involving wireless communication, sensor data acquisition, on-board processing etc.
$\widetilde{E}$	Reduced energy available from battery (J)
E_O	Rated energy available from battery (J)
T_M	Mission Time
T_A	Total stopping time for ancillary functions
$\odot^{[0:end]}$	Value of the quantity $\odot$ from $t = 0$ until end of mission
$\odot^{[t:end]}$	Value of the quantity $\odot$ from $t = t$ until end of mission
$\odot^{[0:t]}$	Value of the quantity $\odot$ from $t = 0$ to $t = t$
$\widehat{[*]}$	Estimated quantity *
$\overline{[*]}$	Average quantity *

tribution in different component so that we know how much energy is used to move the robot. Energy considerations also motivate research in multi-robot coordination. Due to energy constraint, it is always desirable to allocate tasks to robots, which are, if reachable, the closest to the task [19]. However, this also requires an accurate estimate of the achievable range for each individual agent.

Besides those mentioned above, most researchers assume that a robot keeps moving incessantly at a constant velocity, *i.e.*, the robot does not need to stop and process data, but in reality robot might need to occasionally stop to process and send the data. Also, given the resource constraints (fixed battery capacity, limited travel time, limited payload capacity, *etc.*) of a robot, it is also essential to consider resource constrained path planning such that the total path length is bounded. In doing so, we not only respect the resource constraints which are presented inherently while using robots but also ensure that the robot reserves sufficient resources to avoid strangulation.

For exploration mission, the consumed energy could be logically classified into two categories: locomotion and ancillary energy. The former is used to propel the robot into unknown areas. This energy is mostly mechanical and is consumed by physically moving the robot and overcoming the resistance from the environment, such as change of elevation, friction from contact, wind drag, *etc.* The latter is the energy used to replace human presence, such as sensing and communication with peers/base. The current literature focuses more on the impact from the first category, locomotion energy, and thus, could be categorized easily by the type of locomotion model.

2.1. Unmanned Ground Vehicle (UGV)

Unmanned Ground Vehicle (UGV) is the most widely used robotic platform for unknown terrain exploration. Different from other types of platforms, UGV's terramechanics model was well established since the 50′s [5]. Other works include range estimation for Electrical Vehicles (EV) based on a simplified power train model [8,15]. In the robotics field, UGVs' energy are inspected mainly in terms of motion energy [23]. In [9,29], researchers study the necessary energy and remaining battery life based on real-time performance data. Energy consumption minimization techniques have been focusing on trajectory and path planning [16,20,22,37] and high level scheduling [35].

2.2. Unmanned Aerial Vehicle (UAV)

Unlike UGVs, energy related research on Unmanned Aerial Vehicles (UAVs) have started to inspect the flight dynamics and aerodynamics model. [34] looks into energy consumption and range estimation for small fixed wing vehicles based on an aerodynamics model. With the rapid development of rotor-craft, researchers start to inspect the energy related issues in terms of those vertical take-off and landing (VTOL)

platforms. Compared to the well developed terramechanics model, the dynamics for UAVs are still being actively inspected. [4] investigates the effect of different number of rotors on energy consumption of mini UAV. Using an alternative energy source, such as solar energy [18], is another direction of robot design. High level energy consumption strategies are inspected by [10], but as compared to UGV's, there is a vast scope of research in this domain.

2.3. Unmanned Marine Vehicle (UMV)

Unmanned Marine Vehicle (UMV) includes Unmanned Surface Vehicle (USV) and Autonomous Underwater Vehicle (AUV). There is some work on energy harvesting with USVs [21,33]. However, the purpose of using USV is mainly for energy harvesting, not for exploration. Energy related researches are still looking at effective alternative energy sources [3,27,36], including seawater-breathing based on the reaction of powdered aluminum [24] and solar panel [6]. However, some other researchers like Phillips et al. [26] are developing analytical models for deducing optimal cruising speeds of AUV's.

2.4. Limitations of existing works

Most of the aforementioned works either consider the mission profile to be known a priori and then try to estimate/ optimize the energy requirements based on locomotion models only. As opposed to this, it is rather natural to consider the energy itself to be fixed and known a priori given the battery characteristics which serves as the resource constraint, when the robots set out to explore the environment. Thus, we should solve the inverse problem where the energy constraint is known and the path length must be optimized within these constraints. Furthermore, the existing models are made specific to the robot under consideration and to the best of our knowledge, there exists almost no framework generic enough to estimate the operational range of any mobile robot operating on a single discharge cycle. This forms the foundation of our proposed model which considers the locomotion model along with the ancillary functions. Both these consumers draw power from the same source and hence must be accounted for. While doing so, the proposed model is made generic so as to accommodate any robot while retaining the same form.

3. Proposed unified framework

In this section, we explain the novel contributions of this work. So far, standalone researches have looked into development of analytical models for mission energy consumption and duration of specific robotic platforms. Their main focus was to estimate the endurance and energy requirements for robots. Some models were offline whilst others were online built upon real-time operation data. However, one major limitation of these models was that none of them could estimate the maximal operational range of the robot given some a priori known information about the execution of the mission. Furthermore, premeditated trajectories were considered which are not feasible for real-world applications.

Thus, we aim at unifying all such models into one global framework for estimating operational range of a variety of robots. For this, we require the battery characteristics be known which may be additionally supported by a priori mission information, if available. While doing so, we account for variable environmental factors along with the requirements to stop and process the data which in turn affects the maximum attainable range whilst avoiding any premeditated trajectories making our model more pragmatic.

3.1. Energy distribution model for diverse robots

The energy distribution model of our proposed unified framework is shown in Fig. 3: Irrespective of the nature of the robot, the energy available from the battery is always utilized for two kinds of processes

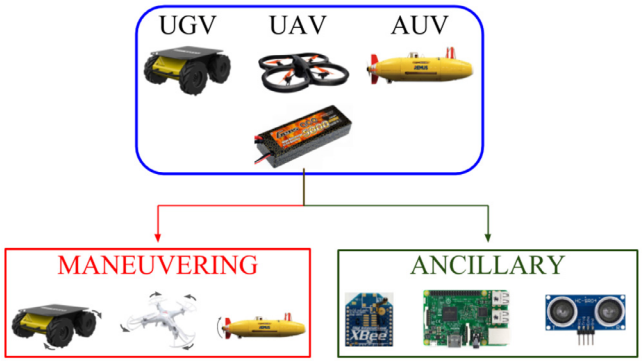

Fig. 3. Energy distribution model for unification framework. Any type of robot, whether a micro UGV, quadrotor UAV, or AUV, uses portable battery packs which are utilized for essentially two functions: *Firstly, maneuvering* like propulsion, hovering, navigation, *etc.* and *secondly*, *ancillary functions* like wireless communication, sensing, on-board processing etc.

viz., maneuvering which we refer to as *propulsive energy* (*PE*) and *ancillary functions* which is referred to as ancillary energy (*AE*). In an ideal situation, the net energy from battery (*E*), *propulsive energy* (*PE*) and ancillary energy (*AE*) are related as:

$$E = AE + PE \tag{1}$$

In reality, owing to several types of losses of capacity, the total energy of the battery is not available as it is. In our prior work, we identified 4 kinds of losses associated with maneuvering and ancillary function modules that, in turn, will affect the maximum attainable range of a mobile robot. They are: battery charge storage loss (η_1), drive motor loss (η_2), mechanical losses owing to internal friction (η_3) and ancillary losses (η_4). So, the overall system efficiency of a robot (r) can be summarized as ${}^{r}\Omega := \Pi_{i=1}^{4} \neg\eta_i$, where $\neg$ operator represents the complement of corresponding losses. The maneuvering efficiency is given by ${}^{r}\Omega_{Man} := \Pi_{i=2}^{3} \neg\eta_i$ and the ancillary efficiency is given by ${}^{r}\Omega_{Anc} := \neg\eta_4$. Here, we have used the zeroth order polynomial *i.e.,* the first order approximation of the efficiency of the system to estimate its lower bound. However, if we used a more complex model (higher order polynomial) that perhaps also accounts for mechanical degradation, changes in current demands owing to variable motor loads, elevation changes and operational velocity modulations *etc.,* better estimates can be obtained. An even higher complexity model could also track the changes in these parameters in real-time which can be used to account for system efficiencies in an *online* fashion and maintain tighter bounds. Having said this, the challenge still remains to identify such models and quantify their parameters. For the scope of this work, we retained only the first order approximation and will investigate the complex counterparts in future works.

As for the *propulsive energy*, any robot (r) carrying out a mission (m) in an environment of choice experiences 4 kinds of forces:

1. Constant resistive force $F(r, m)$ as a function of robot (r) and the mission (m): *e.g.,* the force acting on a robot when it is traversing in a straight line under the influence of a constant magnetic field.
2. Environment dependent force $F(x, r, m)$ which is dependent on the current position x: *e.g.,* changing gravitational potential along with changing frictional force because of change in coefficient of friction.
3. Time dependent resistive force $F(t, r, m)$ which is a function of current time t: *e.g.,* unforeseeable disturbances (strong wind gusts *etc.*).
4. Instantaneous operational velocity dependent resistive force $F(v, r, m)$ which varies with instantaneous velocity v: *e.g.,* aerodynamics and gyro effect.

Thus, the net *propulsive energy (PE)* is given in terms of *mechanical energy (ME)* from longitudinal dynamics model and the net mechanical

efficiency (${}^{r}\Omega_{Man}$) as:

$$\begin{aligned} PE &= \frac{ME}{{}^{r}\Omega_{Man}}, \\ &= \frac{\int_{Path} F_{Net}\,dx}{{}^{r}\Omega_{Man}}, \\ &= \frac{\int_{Path}\{F(r,m)+F(x,r,m)+F(t,r,m)+F(v,r,m)\}dx}{{}^{r}\Omega_{Man}} \end{aligned} \tag{2}$$

Since a robot may occasionally need to stop and process the data, we define a term duty cycle (D) which is the proportion of net mission time that the robot was actually mobile. Then, the duration (t) can be expressed as a function of position (x), velocity (v), mission (m) and duty cycle[3] (D) as:

$$t = g(x, v, D, m) \tag{3}$$

An example of the function $g(\cdot)$ represented by Eq. (3) can be the following. Consider a robot moving with velocity $v = 10m/s$ and a duty cycle of $D = 0.5$. Let the mission (m) be to traverse $10m$ in a straight line. Then, for moving from $x_1 = 0$ to $x_2 = 10m$, the duration, $t = \frac{(x_2 - x_1)}{(vD)}$. During the mission ($m$), we assume that the robot traverses at an instantaneous velocity (v) and a fixed duty cycle (D). Thus,

$$\begin{aligned} PE &= \frac{\int_{Path}\{F(r,m)+F(x,r,m)+F(g(x,v,D,m),r,m)+F(v,r,m)\}dx}{\Omega}, \\ &= \frac{\{F(r,m)+F(v,r,m)\}d}{{}^{r}\Omega_{Man}} + \frac{d\int_{Path}\{F(x,r,m)+F(x,v,D,r,m)\}dx}{d\,{}^{r}\Omega_{Man}} \end{aligned} \tag{4}$$

Moreover, we know that ancillary energy (AE) is given by:

$$AE = \frac{P_{Anc}\,d}{v_{Avg}\,D}, \tag{5}$$

where

$$\begin{aligned} P_{Anc} &= \underbrace{\{s_0 + s_1 f_s\}}_{P_{Sense}} + \underbrace{\{P_{Comp} + P_{Comm}\}}_{P_c} \\ &= \{s_0 + s_1 f_s\} + \{P_{Comp} + k \times |Data| \times f_{Comm}\} \\ &= \{s_0 + s_1 f_s\} + \{P_{Comp} + k \times R\} \end{aligned} \tag{6}$$

As an enhancement for the ancillary power consumption model over our prior work, here, the communication power is related with both the size of the data *i.e.,* $|Data|$, and the frequency (f_{Comm}) at which the communication takes place. These two terms could be unified into data rate (R), *i.e.,* the amount of data sent in unit time. The communication power is then proportional to the data rate with a constant power/data rate coefficient k (*c.f.* [17]). Arguably, the computation power is also a function of the task allocated to the robot, quantifying which, is beyond the scope of our current work. As for the power consumed by sensors given by P_{Sense}, it can be modeled as a function of the sampling frequency f_s. The scalars s_0, s_1 refer to the static power consumption and operational power consumption coefficient respectively.

So, the operational range for any robot can be given in terms of residual energy supplied by battery ($\tilde{E}$) as:

$$d = \frac{\tilde{E}}{\frac{\{F(r,m)+F(v,r,m)\}}{{}^{r}\Omega_{Man}} + \frac{\int_{Path}\{F(x,r,m)+F(\frac{x}{vD},r,m)\}dx}{d\,{}^{r}\Omega_{Man}} + \frac{P_{Anc}}{v_{Avg}D}} \tag{7}$$

Here, ${}^{r}\Omega_{Man}$ is the net maneuvering efficiency of the robot, *i.e.,* the percentage of energy used to do actual mechanical work from the maneuvering branch. From Eq. (7), it is evident that in order to estimate the operational range, we need to approximate the term $\frac{\int_{Path}\{F(x,r,m)+F(\frac{x}{vD},r,m)\}dx}{d\,{}^{r}\Omega_{Man}}$ and the operational range estimate would be as good as the approximation.

[3] Duty cycle (D) refers to the proportion of the mission duration during which the robot was actually moving. For additional details, please refer to Table 1.

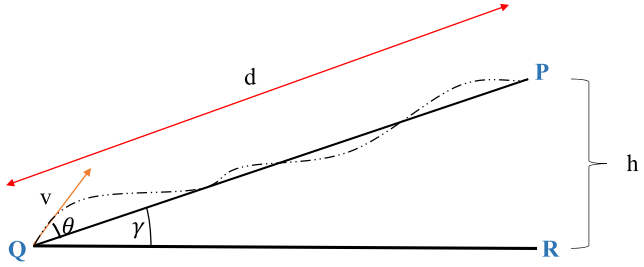

Fig. 4. Schematic of actual terrain profile without rubble. v represents the instantaneous velocity, γ is the average terrain elevation and θ represents instantaneous road gradient with respect to γ. h represents the elevation gain and d represents the operational range.

3.2. Range estimation models for diverse robots

In order to approximate Eq. (7), we propose two different approaches *viz., 1.) Offline* estimation which is a one-shot prediction model wherein we conjecture at the beginning of the mission itself and predictions are not corrected based on the new data acquired, and *2.) Online* estimation whereby we recursively update our estimation using all available operational data. In the conventional setting, *offline* estimates are generated once all the data is made available, while the *online* estimates are limited to the data currently available. As opposed to this setting, the *offline* model being referred to here relies on defining the required parameter values a priori and retaining the estimates. The *online* model on the other hand recursively updates the estimates as more data is made available. Furthermore, for each approach we propose particular models for UGVs and multi-rotor UAVs.

3.2.1. *Approach 1:* Offline *operational range estimation for diverse mobile robot platforms*

We first present an *Offline* model to estimate the operational range applicable to diverse range of unmanned platforms, with the assumption of a priori knowledge of the mission characteristics required for estimation over the entire mission: *e.g.,* average terrain elevation and its variance from the mean value in case of UGVs and average wind compensation angle in case of UAVs.

3.2.1.1. UGV operating in uneven terrain. In our previous work, we considered our operational environment to be a smooth terrain with a constant elevation. However, in this work, we further enhance our model by extending it to uneven terrains with variable elevation making it better suited to real world scenarios.

Any natural terrain can be modeled using three features: *1.) flats:* smooth surfaces with negligible gradient, *2.) slopes:* smooth surfaces with appreciable gradient and *3.) rubble:* uneven rough surfaces with no particular gradient characteristics. The operational terrain may have an average slope (γ) with respect to which the operational range d should be calculated. In Fig. 4, the dashed line represents the actual terrain which must be traversed where QP represents the actual d. QR is the horizontal reference with respect to which the instantaneous road elevation is calculated.

1. Considering *flat* terrains exclusively, the only resistive force acting on the robot is the (rolling) friction between the wheels and the ground. This is defined as:

$$F_{Flats} = Normal\ Force \times C(x)_{rr} \tag{8}$$

where, $C(x)_{rr}$ refers to the coefficient of rolling resistance.

2. Accounting for *slopes*, the net force acting will be friction along with the weight component along the motion of the robot. These forces are a function of the robot location x and the instantaneous terrain elevation at x given by $\theta(x)$.

$$\begin{aligned} F_{Slopes} &= F_{Flats} + m_R g \sin(\gamma + \theta(x)), \\ &= C(x)_{rr} m_R g \cos(\gamma + \theta(x)) + m_R g \sin(\gamma + \theta(x)) \end{aligned} \tag{9}$$

3. Finally, considering *rubble*, in our force model, excess forces (F_{Rubble}) acting due to presence of rubble need to be accounted for. Let $k(x)_{Terr}$ be the terrain coefficient which depends on size, shape, density and resistance offered by the rubble. Then, the net forces (F_{Net}) acting on the robot can be given by:

$$\begin{aligned} F_{Net} &= F_{Slopes} + F_{Rubble}, \\ &:= k(x)_{Terr}(F_{Slopes}) \end{aligned} \tag{10}$$

Thus, the net maneuvering force (${}^{UGV}F(x)_{Man}$) for any UGV on an uneven natural terrain is given by:

$${}^{UGV}F_{Man} = k(x)_{Terr} m_R g[C(x)_{rr} \cos(\gamma + \theta(x)) + \sin(\gamma + \theta(x))] \tag{11}$$

In order to estimate the achievable range d, we first define the total energy model in a real world setting as a sum of Ancillary Energy (AE) and Traversal Energy (TE):

$$\begin{aligned} \tilde{E} &= AE + TE, \\ &= \{Ancillary\ Power \times time\} + \frac{\int_{Path} {}^{UGV}F(x)_{Man} dx}{{}^{UGV}\Omega_{Man}}, \\ &= P_{Anc} \times \frac{d}{v_{Avg} \cos(\theta_{Avg}) D} + \frac{\int_{Path} k(x)_{Terr} m_R g[C(x)_{rr} \cos(\gamma + \theta(x)) + \sin(\gamma + \theta(x))] dx}{{}^{UGV}\Omega_{Man}}, \\ &= P_{Anc} \times \frac{d}{v_{Avg} \cos(\theta_{Avg}) D} + \left\{ \frac{m_R g}{{}^{UGV}\Omega_{Man}} \times \frac{\int_{Path} k(x)_{Terr}[C(x)_{rr} \cos(\gamma + \theta(x)) + \sin(\gamma + \theta(x))] dx \times d}{d} \right\}, \\ &= d \times \left\{ \frac{P_{Anc}}{v_{Avg} \cos(\theta_{Avg}) D} + \frac{m_R g}{{}^{UGV}\Omega_{Man}} \times \frac{\int_{Path} k(x)_{Terr}[C(x)_{rr} \cos(\gamma + \theta(x)) + \sin(\gamma + \theta(x))] dx}{d} \right\}. \end{aligned} \tag{12}$$

Here, d refers to distance covered by the robot. The maximum attainable distance, d_{Max} (operational range) is a function of the optimal velocity v_{Opt}. Cruising at speeds higher/lower than v_{Opt} would result in operational ranges lesser than d_{Max}. So, Eq. (12) can now be written as:

$$d_{Max} = \frac{\tilde{E}}{\frac{P_{Anc}}{v_{Opt} \cos(\theta_{Avg}) D} + \left\{ \frac{m_R g}{{}^{UGV}\Omega_{Man}} \times \frac{\int_{Path} k(x)_{Terr}[C(x)_{rr} \cos(\gamma + \theta(x)) + \sin(\gamma + \theta(x))] dx}{d_{Max}} \right\}}. \tag{13}$$

From Eq. (13), we infer that the factor $\{\frac{m_R g}{{}^{UGV}\Omega_{Man}} \times \frac{\int_{Path} k(x)_{Terr}[C(x)_{rr} \cos(\gamma+\theta(x))+\sin(\gamma+\theta(x))] dx}{d_{Max}}\}$ gives us the average resistive force which acts on the robot on the path QP as shown in Fig. 4. Thus, replacing this factor by the expected average resistive force, we can deduce the d_{Max} and our estimation will be as good as the estimation of the expected average resistive force. As the operational efficiency of the actuators varies with operational speed, v_{Opt} is the velocity at which the net losses of ancillary and maneuvering energy are minimal. Also, as v_{Opt} is a complex function of robot/actuators, exact trajectory traversed or path taken and the mission characteristics, no further comments or profiling of v_{Opt} is possible in the scope of current work. In realistic scenarios, the *offline* model needs the values of $k(x)_{Terr}$, $C(x)_{rr}$ to be defined for each x to find average expected resistive force. Or equivalently, we can eliminate the integral over the path by replacing it with average expected resistive force which can be done by replacing $k(x)_{Terr}$, $C(x)_{rr}$, $\theta(x)$ by their averages $\bar{k}_{Terr}, \bar{C}_{rr}, \bar{\theta}$, respectively. These values for the *offline* model can be estimated using any of the following methods: *1.)* Using the data and experience acquired over the previous missions; *2.)* carrying out a trial mission and then using the acquired information as prior knowledge for the actual mission; *3.)* using the expertise of the operators (system/environment experts) to provide realistic/good estimates. For this work, we have utilized the approach 2.) mentioned above.

3.2.1.2. Multi-rotor UAV operating in presence of external disturbances. Albeit the energy distribution for a UAV is quite similar to that of a UGV as mentioned previously, slight differences still exist. One of the differences is that during the mission, a UGV may have phases of negligible maneuvering energy requirements whilst a UAV continuously needs to hover and maintain flight stability. As opposed to [12], we not only consider the hovering and aerial drag losses but also account for flight adjustments required due to unpredictable environmental factors (like strong wind gusts, *etc.*).

Analogous to the UGVs, the energy for hovering, drag losses and flight adjustments in UAVs are comparable to energy requirements of motion over flats, slopes and rubble respectively. This is owing to the fact that, in case of hovering, the UAV experiences a constant environment dependent force required to stay aloft. Similarly, to maintain motion for a UGV, it must constantly overcome the resistive frictional forces. Identical analogues can also be drawn for remaining cases.

1. For *hovering*, we refer to works of [2]. For a UAV with N_R propellers each of radius r_p with a figure of merit Γ and rotor thrust T_{Hover} in an atmosphere of density ρ, the hovering power (P_{Hover}) can be defined as:

$$\begin{aligned} P_{Hover} &= \frac{(T_{Hover})^{\frac{3}{2}}}{\Gamma r_p \sqrt{2 N_R \rho \pi}}, \\ &= \frac{(m_R g)^{\frac{3}{2}}}{\Gamma r_p \sqrt{2 N_R \rho \pi}} \end{aligned} \tag{14}$$

2. Also accounting for *flight adjustments*[4], the instantaneous power ($P(t)_{fa}$) is given by:

$$P(t)_{fa} = \frac{[T(t)_{fa}]^{\frac{3}{2}}}{\Gamma r_p \sqrt{2 N_R \rho \pi}} \tag{15}$$

[4] The term *flight adjustments* takes into account all adjustments the UAV needs to make in order to maintain its course in presence of external disturbance or otherwise.

where the instantaneous thrust with flight adjustments ($T(t)_{fa}$) is defined as:

$$\begin{aligned} T(t)_{fa} &:= T_{Hover} + T(t)_{Adjust}, \\ T(t)_{Adjust} &= f(t) T_{Controller} \end{aligned} \tag{16}$$

In Eq. (16), $T_{fa}(t)$ refers to the net thrust required for hovering with adjustments. This is defined in terms of hovering thrust (T_{Hover}) and adjustment thrust ($T_{Adjust}(t)$). The term $T_{Controller}$ refers to the thrust required to follow the acceleration profile generated by the chosen flight controller (*e.g.*, PID controller or Neural Networks, *etc.*) and $f(t)$ is a time dependent constant of proportionality. In order to generalize our model and remove the dependence on any particular flight controller, we choose to model T_{Adjust} as a time dependent function of T_{Hover} as:

$$T(t)_{Adjust} := k(t)_{Env} T_{Hover}. \tag{17}$$

Here, $k(t)_{Env}$ is the constant of proportionality. Thus,

$$\begin{aligned} T(t)_{fa} &= T_{Hover} + k(t)_{Env} T_{Hover}, \\ &= m_R g + k(t)_{Env} m_R g. \end{aligned} \tag{18}$$

$$P(t)_{fa} = \frac{\left[m_R g + k(t)_{Env} m_R g\right]^{\frac{3}{2}}}{\Gamma r_p \sqrt{2 N_R \rho \pi}} \tag{19}$$

So, the average power for *flight adjustments* over the entire time of flight (*TOF*) is given by:

$$P_{fa} := \frac{\int_{TOF} \left[\{m_R g + k(t)_{Env} m_R g\} dt\right]^{\frac{3}{2}}}{TOF\ \Gamma r_p \sqrt{2 N_R \rho \pi}} \tag{20}$$

3. Finally, we incorporate *drag losses* acting on rotor blades. The drag force (F_D) on N_R propellers, with drag coefficient C_D, cross-section area A and velocity v is estimated from fluid mechanics as:

$$\begin{aligned} F_D &= \frac{N_R \rho C_D A v^2}{2}, \\ &= \frac{N_R \rho C_D A (r_p \omega)^2}{2}. \end{aligned} \tag{21}$$

where, r_p is the propeller radius and ω is its angular velocity. The drag torque (τ_D) is given by:

$$\begin{aligned} \tau_D &= \int_0^{r_p} F_D dr, \\ &= \frac{N_R \rho C_D A r_p^3 \omega^2}{6} \end{aligned} \tag{22}$$

Since the power required to overcome the drag losses is given by $\tau_D \omega$ and we know that drag thrust $T(t)_{fa} (= N_R k_r \omega^2)$ for the propeller constant k_r, we can define the instantaneous power for drag losses ($P_D(t)$) as:

$$P_D(t) = \frac{\rho C_D A r_p^3 [T(t)_{fa}]^{\frac{3}{2}}}{6 k_r \sqrt{N_R}} \tag{23}$$

Substituting Eqs. (18) into (23), we get:

$$P_D = \frac{\rho C_D A r_p^3 [\int_{TOF} \{m_R g + k(t)_{env} m_R g\} dt]^{\frac{3}{2}}}{6 k_r \sqrt{N_R}\ TOF} \tag{24}$$

The net energy required for navigation of a UAV is now given based on Eq. (12) as:

$$\begin{aligned} \tilde{E} &= AE + TE, \\ &= Ancillary\ Power \times TOF + \frac{[P_D + P_{fa}] TOF}{{}^{UAV}\Omega_{Man}}, \\ &= P_{Anc} \times TOF \\ &\quad + \frac{\frac{\rho C_D A r_p^3 [\int_{TOF} \{m_R g + k(t)_{Env} m_R g\} dt]^{\frac{3}{2}}}{6 k_r\ TOF \sqrt{N_R}} + \frac{\int_{TOF} \left[\{m_R g + k(t)_{Env} m_R g\} dt\right]^{\frac{3}{2}}}{TOF\ \Gamma r_p \sqrt{2 N_R \rho \pi}}]}{{}^{UAV}\Omega_{Man}}, \\ &= P_{Anc} \times TOF \\ &\quad + \left\{ \frac{\left[\frac{\rho C_D A r_p^3}{6 k_r \sqrt{N_R}}\right] + \left[\frac{1}{\Gamma r_p \sqrt{2 N_R \rho \pi}}\right]}{{}^{UAV}\Omega_{Man}} \right\} \left\{ \frac{\int_{TOF} \left[\{m_R g + k(t)_{Env} m_R g\} dt\right]^{\frac{3}{2}}}{TOF} \right\} TOF \end{aligned} \tag{25}$$

Rearranging the terms in Eq. (25), we get:

$$TOF = \frac{\tilde{E}}{P_{Anc} + \left\{ \frac{\left[\frac{\rho C_D A r_p^3}{6 k_r \sqrt{N_R}}\right] + \left[\frac{1}{\Gamma r_p \sqrt{2 N_R \rho \pi}}\right]}{{}^{UAV}\Omega_{Man}} \right\} \left\{ \frac{\int_{TOF} \left[\{m_R g + k(t)_{Env} m_R g\} dt\right]^{\frac{3}{2}}}{TOF} \right\}} \tag{26}$$

Replacing $TOF = \frac{d_{Max}}{v_{Opt}}$ in Eq. (26), we obtain:

$$\begin{aligned} d_{Max} &= \frac{\tilde{E}}{\frac{P_{Anc}}{v_{Opt} D} + \left\{ \frac{\left[\frac{\rho C_D A r_p^3}{6 k_r \sqrt{N_R}}\right] + \left[\frac{1}{r_p \sqrt{2 N_R \rho \pi}}\right]}{{}^{UAV}\Omega_{Man} v_{Opt}} \right\} \left\{ \frac{\int_{TOF} \left[\{m_R g + k(t)_{Env} m_R g\} dt\right]^{\frac{3}{2}}}{TOF} \right\}}, \\ &\because D = 100\%\ \text{for UAV}, \\ d_{Max} &= \frac{\tilde{E}}{\frac{P_{Anc}}{v_{Opt}} + \left\{ \frac{\left[\frac{\rho C_D A r_p^3}{6 k_r \sqrt{N_R}}\right] + \left[\frac{1}{r_p \sqrt{2 N_R \rho \pi}}\right]}{{}^{UAV}\Omega_{Man}} \right\} \left\{ \frac{\int_{TOF} \left[\{m_R g + k(t)_{Env} m_R g\} dt\right]^{\frac{3}{2}}}{TOF\ v_{Opt}} \right\}}, \end{aligned} \tag{27}$$

From Eq. (27), the factor $\{\frac{\frac{\rho C_D A r_p^3}{6 k_r \sqrt{N_R}} + \frac{1}{\Gamma r_p \sqrt{2 N_R \rho \pi}}}{{}^{UAV}\Omega_{Man}}\}$ $\{\frac{\int_{TOF} [\{m_R g + k(t)_{Env} m_R g\} dt]^{\frac{3}{2}}}{TOF\ v_{Opt}}\}$ represents the average resistive force experienced by the UAV over the entire time of flight. This is akin to Eq. (13) which serves to justify our claim of a *unified framework*. An apt replacement of this parameter by using the expected average resistive force can help to estimate the maximum operational range for the UAV. The error in estimation of this factor directly translates to the error in expected operational range and can be estimated using the same methods as mentioned in the case of UGV.

3.2.2. *Approach 2:* Online *operational range estimation for diverse mobile robot platforms*

Previously, we introduced an *offline* range estimation model, whereby, based on a priori known mission characteristics, we can estimate the maximum attainable range for mobile robots. However, in reality, it might be rather challenging to strictly follow the mission characteristics or to even obtain a priori mission information. In order to adapt to such situations, we now propose an *online* variant of our operational range estimation framework. In this method, based on all available real-time data, the operational range is recursively updated.

3.2.2.1. UGV operating in uneven terrain. In Eq. (13), the terms $k(x)_{Terr}$ and $\theta(x)$ can either be set by a human operator (offline model) or can be deduced from prior missions carried out in that terrain. However, the former introduces human error and the latter is usually not available. Thus, as an alternative, we now replace $k(x)_{Terr}$, $\theta(x)$ by their respective

estimates, $\hat{k}(x)_{Terr}, \hat{\theta}(x)$. Additionally, the *offline* model used instantaneous rolling resistance $C_{rr}(x)$ while here it is being approximated by a constant C_{rr}. So, the estimated maximum range for the remaining mission is now given by:

$$\hat{d}_{Max}^{[t:end]} := \frac{\tilde{E}_{Rem}}{\frac{P_{Anc}}{v_{Opt} D} + \frac{\hat{k}(x)_{Terr}[C_{rr}\cos\hat{\theta}(x) + \sin\hat{\theta}(x)]m_R g}{UGV\,\Omega_{Man}}}, \tag{28}$$

where

$$\tilde{E}_{Rem} = \tilde{E}^{[0:end]} - \tilde{E}^{[0:t]} \tag{29}$$

Here, $\tilde{E}_{Rem}$ is the useful energy remaining in the battery and $\tilde{E}^{[0:end]}$ is the usable energy present in the battery at the start of the mission, *i.e,* at $t = 0$. Similarly, $\tilde{E}^{[0:t]}$ is the energy spent from $t = 0$ to time instance t. Now, the total estimated maximum operational range over the entire mission is given by:

$$\hat{d}_{Max}^{[0:end]} = d^{[0:t]} + \hat{d}_{Max}^{[t:end]} \tag{30}$$

In Eq. (30), to estimate the net operational range for the entire mission ($\hat{d}_{Max}^{[0:end}$]), we need to utilize the distance that has already been covered ($d^{[0:t]}$) and estimate the maximum distance that may be covered ($\hat{d}_{Max}^{[t:end]}$) based on available residual energy. The value of $\hat{k}(x)_{Terr}$ that is required for estimating $\hat{d}_{Max}^{[t:end]}$ can be estimated using Eq. (28). During the mission, after every time-step (t), the robot will have the knowledge of the distance that it has covered in that time-step, energy it has spent to cover that distance and terrain elevation θ for that time step. Substituting the value of $d^{[t-1:t]}$ for d_{Max} and $E^{[t-1:t]}$ for $\tilde{E}_{Rem}$ in Eq. (28), we can calculate the value of $k(x)_{Terr}^{[t]}$ for the given time-step t. Now, these set of values of $k(x)_{Terr}^{[t]}$ can be used to estimate $\hat{k}(x)_{Terr}$ which in turn can be used to make predictions about the distance the robot can still cover using the remaining energy. Since the estimate for the remaining distance depends upon the value on the estimation of $\hat{k}(x)_{Terr}$ and $\hat{\theta}(x)$, which needs to be recursively updated as new data is being collected, we utilize a recursive average filter. For ease of notation, we define $\hat{\mathbf{X}}^{[t]} = [\hat{k}(x)_{Terr}^{[t]}, \hat{\theta}(x)^{[t]}]$ and $\mathbf{Z}^{[t-1]} = [k(x)_{Terr}^{[t-1]}, \theta(x)^{[t-1]}]$ which represents the set of actual (noisy) measurements up till the last time step ($t-1$).

Then, given a noisy set of measurements, $\mathbf{Z}^{[0:t-1]}$, and no additional information about the impact of environmental factors on the system dynamics, a reasonable estimate for the system state at the current time-step, t can be obtained as:

$$\hat{\mathbf{X}}^{[t]} = P^{[t-1]} \sum_{i=0}^{t-1} \mathbf{Z}^{[i]} \tag{31}$$

where $P^{[t-1]} = \frac{1}{t-1}$ represents the responsiveness of the filter, *i.e.,* the filter is very responsive (making a lot of corrections) in the beginning since limited data is available. As time passes and more data becomes available, the filter becomes more certain about its estimates, and thus, reduces the relative importance of the measurements. However, being a fixed response model (true values of k_{Terr} and θ_{Terr} are fixed) with response rate decreasing with time, it cannot always adapt to sudden changes in the values of $k(x)_{Terr}$ and $\theta(x)_{Terr}$ as $\frac{1}{t-1}$ can be very small. These sudden changes can occur when there is a change in terrain type or weather conditions, however their impact is diminished with the passage of time. We can now manipulate Eq. (31) to obtain the recursive update rule as follows:

$$\begin{aligned}
\hat{\mathbf{X}}^{[t]} &= P^{[t-1]} \sum_{i=0}^{t-1} \mathbf{Z}^{[i]} \\
&= P^{[t-1]} \sum_{i=0}^{t-2} \mathbf{Z}^{[i]} + P^{[t-1]} \mathbf{Z}^{[t-1]} \\
&= \frac{t-2}{t-1} \times \underbrace{\frac{1}{t-2} \sum_{i=0}^{t-2} \mathbf{Z}^{[i]}}_{\hat{\mathbf{X}}^{[t-1]}} + P^{[t-1]} \mathbf{Z}^{[t-1]} \\
&= \hat{\mathbf{X}}^{[t-1]} + P^{[t-1]} \left(\mathbf{Z}^{[t-1]} - \hat{\mathbf{X}}^{[t-1]} \right)
\end{aligned} \tag{32}$$

Eq. (32) represents the recursive state update rule wherein the term $P^{[t-1]}(\mathbf{Z}^{[t-1]} - \hat{\mathbf{X}}^{[t-1]})$ represents the *measurement innovation i.e.,* the new information acquired via the new observation. Similarly, the recursive update rule for the filter response can also be derived as:

$$P^{[t]} = P^{[t-1]} - P^{[t-1]}(P^{[t-1]} + 1)^{-1} P^{[t-1]} \tag{33}$$

From Eqs. (32) and (33), it is clear that our filter is a modified moving average filter [30] with increasing window size, that accommodates all the data available. The predictions begin at $t = 2$, and $\hat{\mathbf{X}}^{[1]} = \mathbf{Z}^{[1]}$. Here, we can see that $\mathbf{X}^{[t]}$ is a function of $\mathbf{Z}^{[0:t-1]}$ which is a series of points indexed in time order *i.e.,* a time-series. So we can use common time-series forecasting method to estimate the value of $\mathbf{X}^{[t]}$ such as various variants of Autoregressive moving average (ARMA) model [13]. In our case, we have used a modified moving average model (ARMA(0,0,1)), that computes the average of all the data points available to estimate the value of $\mathbf{X}^{[t]}$.

3.2.2.2. Multi-rotor UAV operating in presence of external disturbances. Similar to the case of UGVs, we now replace the term $k(t)_{Env}$ in Eq. (27) by its estimated value $\hat{k}(t)_{Env}$. Thus, the estimated maximum range for UAV for remainder of the mission is now given by:

$$\hat{d}_{Max}^{[t:]} := \frac{\tilde{E}_{Rem}}{\frac{P_{Anc}}{v_{Opt}} + \left\{ \frac{\left[\frac{UAV\,\Omega_{Man}\rho C_D A r_p^3}{6k_r\sqrt{N_R}} \right] + \left[\frac{1}{r_p\sqrt{2N_R\rho\pi}} \right]}{UAV\,\Omega_{Man} v_{Opt}} \right\} [m_R g + \hat{k}(t)_{Env} m_R g]^{\frac{3}{2}}} \tag{34}$$

Now, the maximum operational range estimation can be done similar to Eqs. (30) and (32). However, in case of UAV, we define $\hat{X}^{[t]} = \hat{k}(t)_{Env}$ and $Z^{[t-1]} = k(t-1)_{Env}$ as the estimated and observed values of the environmental variable which are required for operational range estimation.

4. Experiments

In this section, we present the details of the robotic platforms used for empirical validations of the unified framework proposed, followed by empirical analysis of results thus obtained.

4.1. Robot platforms

First, we explain the robotic platforms that were used for our model verification along with their corresponding parameters that are used by our frameworks.

4.1.1. Unmanned Ground Vehicle (UGV)

For the ground robot, we assembled a custom robot from readily available off-the-shelf components which was named as *Rusti V2.0*. As an enhancement over its predecessor showcased in our prior work, this now has a stronger alloy frame and powerful $12V$ DC geared motors. We mounted a Raspberry Pi 3 kit on-board which can receive control commands from the human operator using wired Double Pole Double Throw (DPDT) switches. In order to gather the accelerometer data, we used the *Empatica E4* wristband which measured the GSR and HR [11] using its independent power source. This wearable sensor records multiple physiological signals but since the scope of this study is limited to the accelerometer, the readings from other sensors were not processed. Thus, our accelerometer data was logged separately and was later fused with other information for analysis. As for the ancillary functions, we connected the $HC-SR04$ Ultrasonic ranging module with a non-contact detection range of $(2-400) \pm 0.3$ cm[5]. Our UGV weighing around $3.10\,Kgs$ is shown in Fig. 5.

4.1.2. Unmanned Aerial Vehicle (UAV)

The Parrot ARDrone 2.0 quadrotor platform was used for our UAV related experiments as shown in Fig. 6. It has $N_R = 4$ rotors, each with a

[5] taken from http://www.micropik.com/PDF/HCSR04.pdf.

(a) Outdoor experiments on asphalt (b) Outdoor experiments on grass (c) Outdoor experiments on tiles

Fig. 5. Rusti V2.0 with all-terrain wheels and external 3-axis accelerometer sensor for outdoor field experiments carried out on different terrains.

Fig. 6. Ardrone 2.0 with GPS used for outdoor experiments.

radius of $r_p = .1016m$. The average propeller efficiency ${}^{UAV}\Omega_{Man} = 0.27$ was taken based on multiple experimental evaluations as showcased in [1]. The nominal operational voltage of the high density 1500 *mAH* battery for ARDrone is 11.1*V*. We mounted a GPS sensor which operates at 500 *mA* @ 5 *V*. The maximum rpm of the motor is 41400 while for hovering is 28500 *rpm* with a gear ratio of 2:17 with the propellers. The mass of ARDrone was found to be 0.46 *Kgs*.

4.2. System identification

Before we proceed to present our results of the field experiments, we need to obtain the system parameters *i.e.,* efficiency of *ancillary* and *maneuvering* branches.

For the *Rusti V2.0*, the battery charge storage losses (η_1) were found to be negligible (0.5%) (based on our prior work) while the motor losses (η_2) and mechanical losses (η_3) were deduced based on wheels-up test. For this test, we simply connect the motors to the battery and Raspberry pi to a stepped down 5*V* supply via a voltage regulator. We then let the motors run until the battery is completely drained and based on the logged data we can calculate the motor losses. These losses thus combine the losses incurred owing to motor itself and the heat losses from the motor driver. Since there were no significant heat loss from any electronics component used on-board, we assume the ancillary losses $\eta_4 \approx 0$.

For the *ARDrone*, like the UGV case, the battery charge storage losses (η_1) were taken to be negligible (0.5%). Motor efficiency (η_2) can be deduced from Fig. 4 of [14]. However, monitoring real time RPM of the motors for empirically estimating motor losses is rather challenging. Thus, we use the data for another similar motor which matches the specifications of the ARDrone motor as closely as possible. The average propulsion system efficiency (*i.e.,* combined motor efficiency (η_2) and propeller efficiency (η_3)) was derived based on several experiments and was reported to be equal to 0.27 in [1]. The ancillary losses were taken to be negligible ($\eta_4 \approx 0$) in this case.

4.3. Outdoor experiment setup

Now we explain the navigation conditions in which the two robots were evaluated. For the UGV, we performed 36 experiments on various terrains comprising of either grass, tiles, or asphalt with varying elevations and wheel rpm of 80 and 140[6] Due to space limit, only 12 experiments are plotted and shown in this paper. The reason for considering these terrain types individually was the lack of capable hardware to determine change in terrain types on-the-fly and accordingly adjust the coefficient of rolling friction for making online prediction. We performed 6 *wheels-up* tests at 100 and 200 rpm for system identification. The average rolling coefficients for terrain resistance offered by grass, tiles, and asphalt were set as 0.099,0.066, and 0.062, respectively and the prior information of γ to be used in the *offline* estimation was set based on Table 1 of [29]. In order to deduce the average values of the parameters, we used $\overline{k}_{Terr}^{[0:t]} \leftarrow \frac{\bar{E}^{[0:t]} - AE^{[0:t]}}{F_{Slopes}}$. Similarly, the equations for $\overline{\gamma}^{[0:t]}, \overline{\theta}^{[0:t]}$ can be deduced.

As for the UAV, we performed 30 experiments split into two different sets, *viz., hovering* and *motion*. Only 5 of those experiments are plotted and shown in Fig. 12. For *hovering*, only the altitude of the UAV was varied and the human operator occasionally had to send control commands to maintain the position of the drone within a set perimeter. As opposed to this, in *motion* case, the human operator constantly fed linear motion commands to the drone whilst occasionally commanding the drone to hover (in cases when wind gusts lead to dangerously high velocity gains). This not only helped ensure the safety of the drone and its operator but also helped emulate the real life scenarios in which the drone may loose connection to the base station or corruption of mission critical information. The control commands were sent at operator-defined data transmission rate such that the P_{Comm} in Eq. (6) remained constant. We performed 10 experiments for *hovering* at different altitudes varying between [1,10] meters. Furthermore, we conducted 20 experiments at 5 different operational velocities[7] for *motion* to account for a mix of

[6] Given the wheel radius of 65*mm*, these translate to $v = 0.544, 0.952$ m/s respectively. The velocities were pre-set at the beginning of the field trial and were not monitored during the field trial. For *offline* and *online* models, the heading velocity remained constant and for turning, while one side of motors were slowed by δ, the other side was sped up by the same factor. This ensured that the average velocity of the center of mass of the robot remained constant.

[7] The translation velocities were chosen from [0.1,0.2,0.4,0.6,0.8] m/s which are subject to brief change upon change in heading direction. *E.g.,* consider

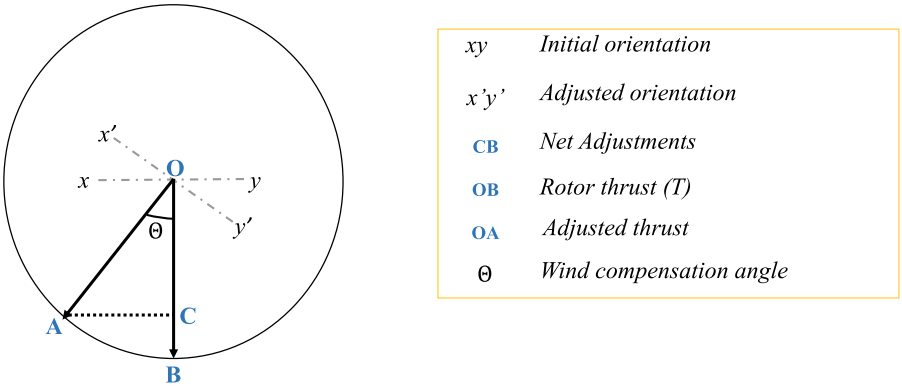

Fig. 7. Geometric analysis of wind compensation angle to deduce the value of parameter $k(t)_{Env}$. Suppose the UAV is stable, then the orientation is represented by *xy* and *OB* represents the thrust (*T*) exerted by the UAV for maintaining flight. Now let us assume that because of sudden wind action, the rotorcraft is displaced by an angle θ (which can also be interpreted as wind compensation angle) and the new orientation is *x′y′*. So, *OA* will represent the same thrust under the sudden influence of the wind at an angle θ to the previous direction. Thus, the net altitude destabilization effect of the wind is given by *BC*.

wind gusts, altitude adjustments, variable mission speeds, and trajectories. Experiments were performed at intervals of 2 hrs so as to account for changing environmental factors like wind and weather conditions.

In our experiments, we constantly monitored the wind compensation angle of the UAV. Through simple geometry, this was then used to calculated real-time values of $k(t)_{Env}$ as explained in Fig. 7. From this figure, we know that the net stabilization required on the part of the rotorcraft will be $CB = OB(1 - \cos(\theta))$. When the rotorcraft was maintaining a constant altitude, the value of $OB = m_R g$. So here *CB* represents $k(t)_{Env} m_R g$ as explained in Eq. (17). Therefore, we get $k(t)_{Env} = 1 - \cos(\theta)$.

From Eqs. (13) and (27), we can see that to make predictions of d_{Max}, we need to have an estimate of average resistive forces, for which value of factor $k(x)_{Terr}$ or $k(t)_{Env}$ is required. So, to make predictions in real-time, we need to recursively update our estimates of these factors. Thus, the proposed filter is fed with real time mission data to update these parameters recursively.

4.4. Batteries used for field experiments

Since the *ARDrone* comes factory fitted with a mini-tamiya connector we used the $11.1V$@$1500mAh$ high density LiPo battery for it. However, having custom built the *Rusti V2.0*, we had the freedom to use the following 2 LiPo batteries for our experiments:

- $11.1V$@$2200mAh$
- $11.1V$@$1500mAh$ (also used for *ARDrone*)

4.5. Empirical results

The following section provides factual performance of our framework in real world operations. Besides these, we also provide other interesting conclusions that can be drawn from these experiments (Figs. 8–10).

4.5.1. Rusti V2.0

In Figs. 8–10, we analyse the performance of our *offline* and *online* models during real field trials on grass, asphalt, and tiles, respectively. For *offline* estimation, we know from Eq. (13) that for estimating the operational range our model needs prior information about θ, γ, and k_{Terr}. Also, the mechanical efficiency[8] is unascertained. For γ, we fixed the value based on Table 1 of [29], and empirically set the values of θ_{Avg} to 5°. Estimating the values of k_{Terr} and ${}^{Rusti}\Omega_{Man} = \Pi_{i=2}^{3} \neg\eta_i$ are rather challenging and require some prior field experience. So, for estimating these, we modified Eq. (13) to bring efficiency within the integral and treated $\frac{k_{Terr}}{{}^{Rusti}\Omega_{Man}}$ as a single terrain dependent variable. The average value of this terrain dependent factor was then determined through a series of field trials as $\frac{k_{Terr}}{{}^{Rusti}\Omega_{Man}} = [3.09, 2.81, 2.69]$ for grass, asphalt, and tiles, respectively. For *online* estimation, the belief of the model over the net operational range achievable is updated in real-time based on cumulative performance characteristics. Effectively, on an average, the net true distance covered by the robot at $0.544m/s$ and $0.952m/s$ are almost the same on all types of terrain. This can be attributed to the fact that because of the use of high torque dc motors in our robot *Rusti*, the net ancillary energy requirements are negligible compared to maneuvering energy (which is independent of operational speed). From Eq. (13) we see that this in fact will be the case if $P_{Anc} \ll P_{Man}$. Also, the true distance covered using the $2200mAh$ battery is greater than that covered using the $1500mAh$ battery but they are not in proportion of the battery capacities i.e. the ratio of battery capacities is $\frac{22}{15} = 1.47$ but the ratio of achieved true range is $\frac{6.67}{5.17} = 1.29$. This difference can be attributed to the fact that the mass of the robot is slightly higher when using the $2200mAh$ battery which dilutes the effect of extra charge capacity.

Then in Fig. 11, we evaluate the accuracy of both our *offline* and *online* models. As was expected, the *offline* model tends to over-shoot or under-shoot the true operational range incurring extreme errors with high variance[9] whilst the *online* models tends to attain the true operational data with a very high accuracy and low variance. It must be pointed out here that while traversing on grass using the following settings: $1500mAh$@$0.952m/s$, both the models show comparable average performance while for $2200mAh$@$0.952m/s$ the *offline* model performs slightly better. Despite this, the variance of the *offline* model remains higher which can also be confirmed from Fig. 8. Overall, the *online* model shows $\approx 60\%$ enhanced accuracy as compared to its adversary for operational range estimation of Rusti V2.0.

4.5.2. Ardrone 2.0

In Fig. 12, we demonstrate the real world performance of our *offline* and *online* estimator models:

For *offline* estimation, prior information regarding the operational environment of the robot is required to make meaningful predictions of its operational range. Since there is no prior research explaining how the values of the parameter $k(t)_{Env}$ vary, we performed an additional set of 5 experiments (each in varying conditions) and averaged their data for estimating the value of the parameter $k(t)_{Env}$ which was found to

operational velocity of 0.1 m/s along $+X$ direction. Upon request to change direction to $-X$, the velocity during this brief transition period will vary from 0.1 m/s in $+X$ to 0 m/s in $+X$ followed by 0.1 m/s in $-X$ direction. This velocity profile cannot be feasibly estimated for *offline* model, so we directly used the operational velocity (0.1 m/s for this *e.g.*), while for the *online* model, velocity was continuously observed, so the average velocity till current time step was used.

[8] ${}^{Rusti}\Omega_{Man}$ is dependent only on the motors and will account for both frictional losses as well as heat losses in motor

[9] **N.B.**: The readers are hereby cautioned that the said variance is the variance in the performance of the *online* filter over multiple trials. This must not be confused with the variance in the forecasting capabilities of the filter during an experiment. As for the *offline* filter, there is a large bias.

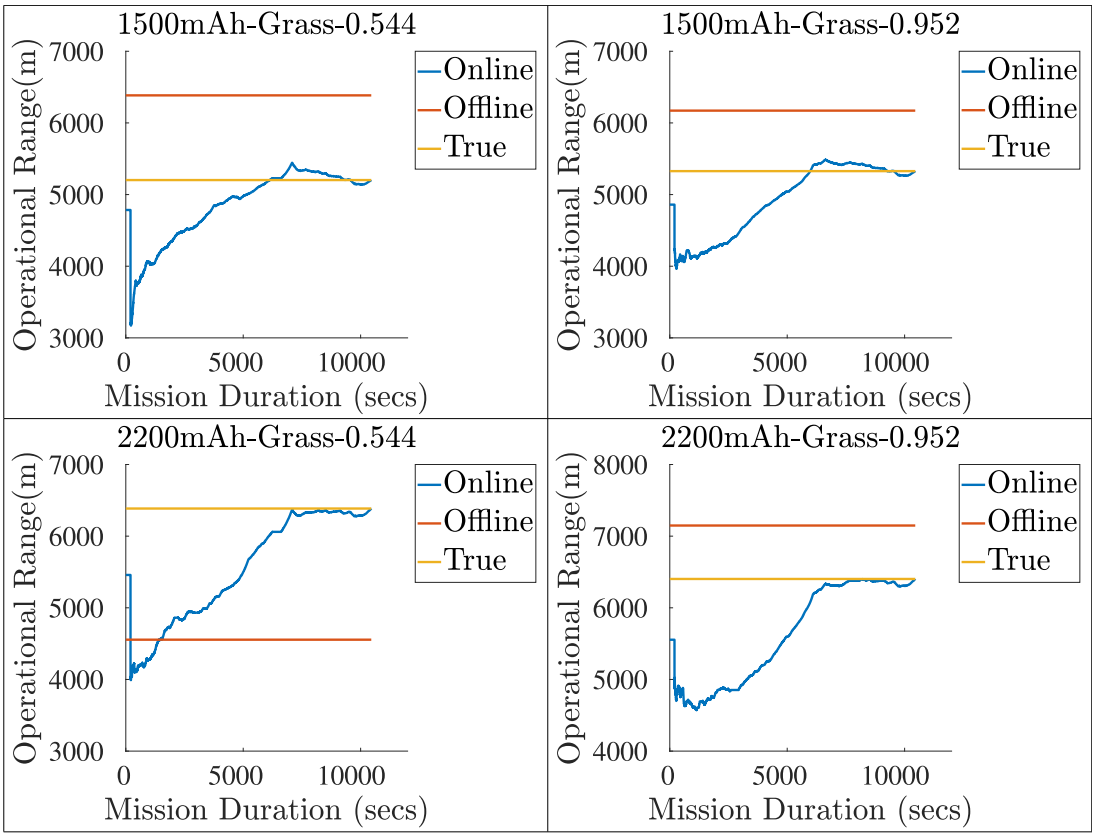

Fig. 8. Rusti's operational range estimation for grass. Top row represents experiments performed using 11.1*V*@1500*mAh* battery @80*rpm* followed by @140*rpm*. Bottom row represents the similar pattern for 11.1*V*@2200*mAh* battery respectively.

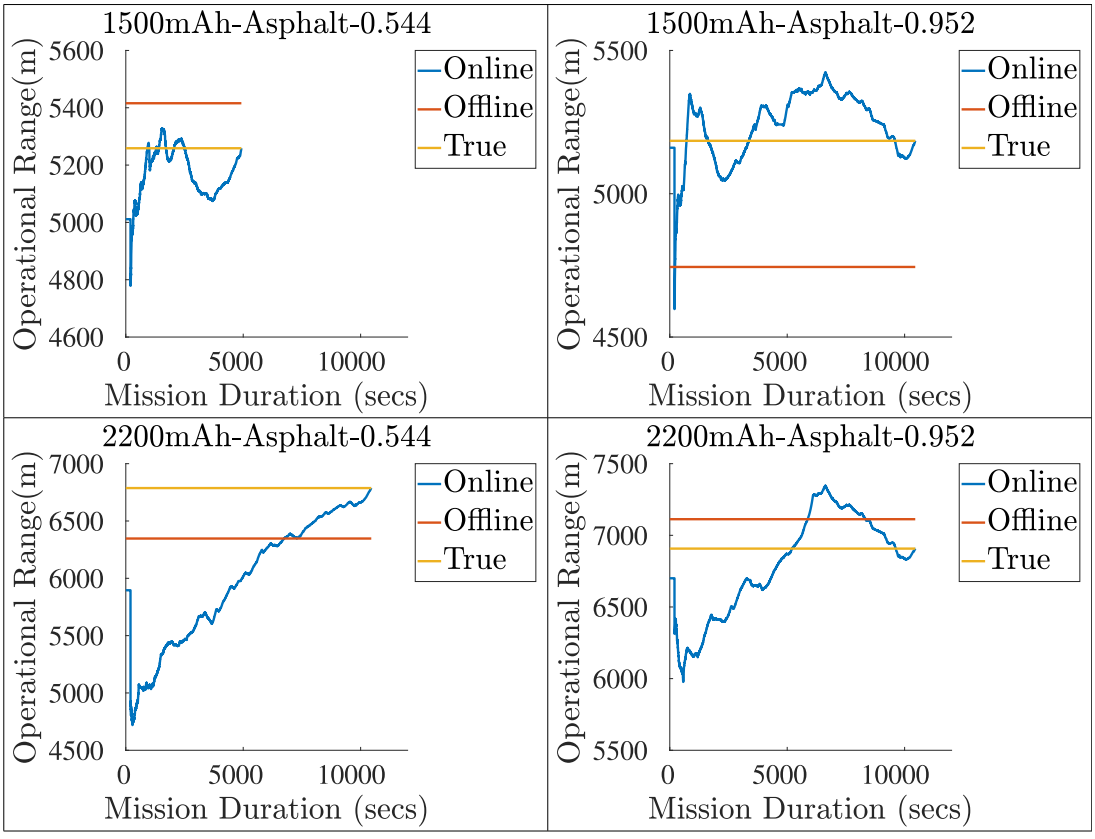

Fig. 9. Rusti's operational range estimation for asphalt. Top row represents experiments performed using 11.1*V*@1500*mAh* battery @80*rpm* followed by @140*rpm*. Bottom row represents the similar pattern for 11.1*V*@2200*mAh* battery respectively.

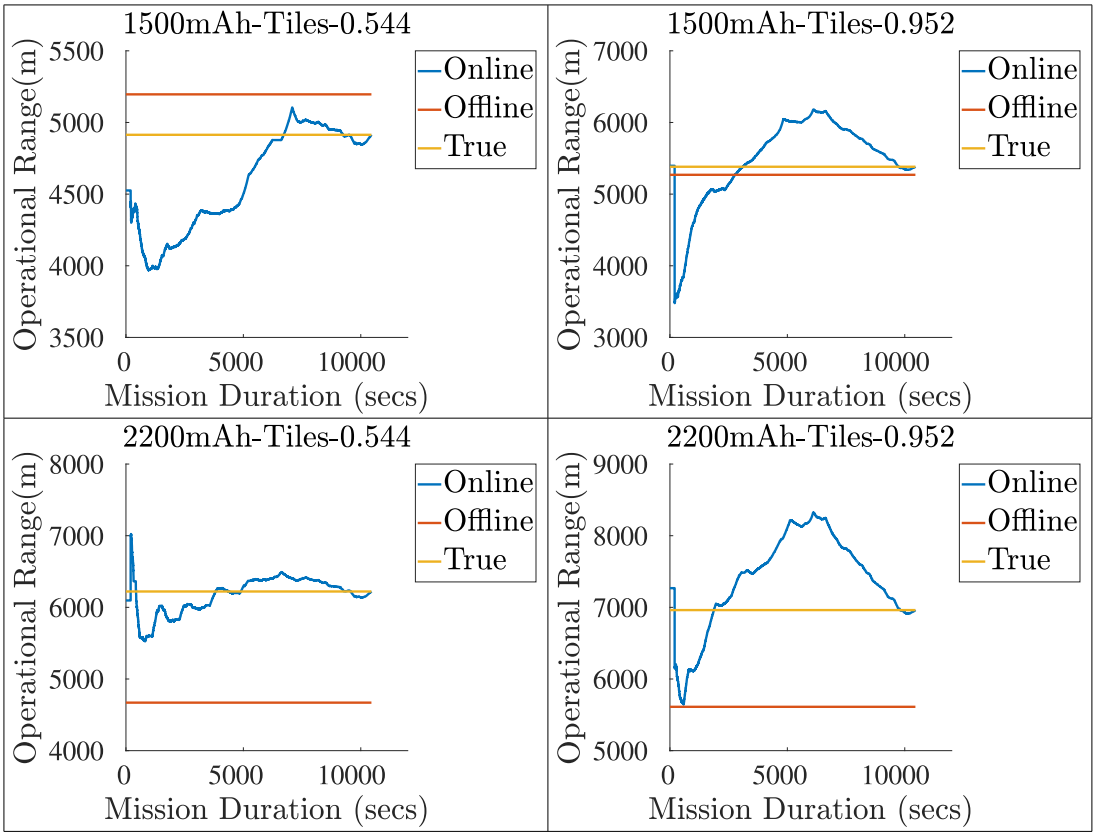

Fig. 10. Rusti's operational range estimation for tiles. Top row represent experiments performed using 11.1*V*@1500*mAh* battery @80*rpm* followed by @140*rpm*. Bottom row represents the similar pattern for 11.1*V*@2200*mAh* battery respectively.

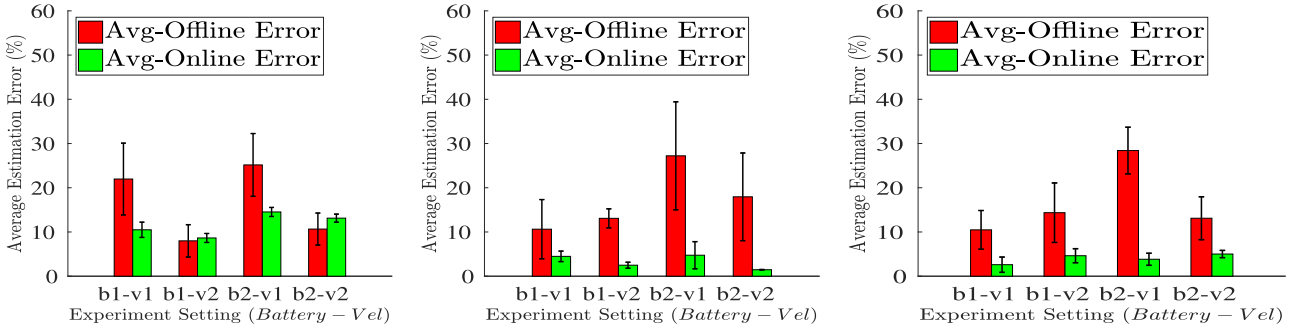

(a) Range estimation error on grass (b) Range estimation error on asphalt (c) Range estimation error on tiles

Fig. 11. Range estimation error for Rusti while traversing on grass, asphalt and tiles. Here $b1$, $b2$ refer to the 1500mAh and 2200mAh batteries and $v1, v2$ refers to 0.544,0.952 m/sec velocities respectively.

be ≈ 0.01. Using this prior information, we estimated the operational range using the *offline* model in the 20 experiments presented here. As the mean estimation error for the *offline* model is about 30 meters in each experiments, with even lower errors at slower speeds, the value of $k(t)_{Env} = 0.01$ is claimed to be optimal.

For *online* estimation, the estimate of the net operational range is updated recursively using mission data acquired in real time. We do not explicitly provide a priori known mission information to deduce the value of the parameters $k(t)_{Env}$ and v. Instead, they are deduced based on real-time mission information. When deploying this model in real life, we can set the prior mission information based on the information gathered in that terrain/field from previous experiments. If no previous experiment data is available, then, the first few values can be used to generate a prior knowledge. For this work, we utilized the initial set of samples as the prior information for the *online* model. We refer to the initial instability in the Ardrone and the sensor's data, just after takeoff, as the burn-in phase. The data of the burn-in phase is discarded and the *online* estimation frameworks is activated only upon Ardrone's stabilization. For the purpose of continuous representation in graphs, the data was interpolated during this phase resulting in the initial straight line trends observed during the burn-in phase of the plots. Also, as is evident from the plots, the *online* estimator converges to the true distance as the mission progresses. As more and more mission data becomes available, the estimation performance of the *online* model becomes significantly better than its *offline* counterpart.

It must also be pointed out here that the variations in the *online* estimator are quite profound during the early stages of the mission which can be attributed to the fact that the estimator is trying to update its belief with sparse and limited amount of data, but it quickly stabilizes as the amount of data grows. Also, it might seem that increasing the

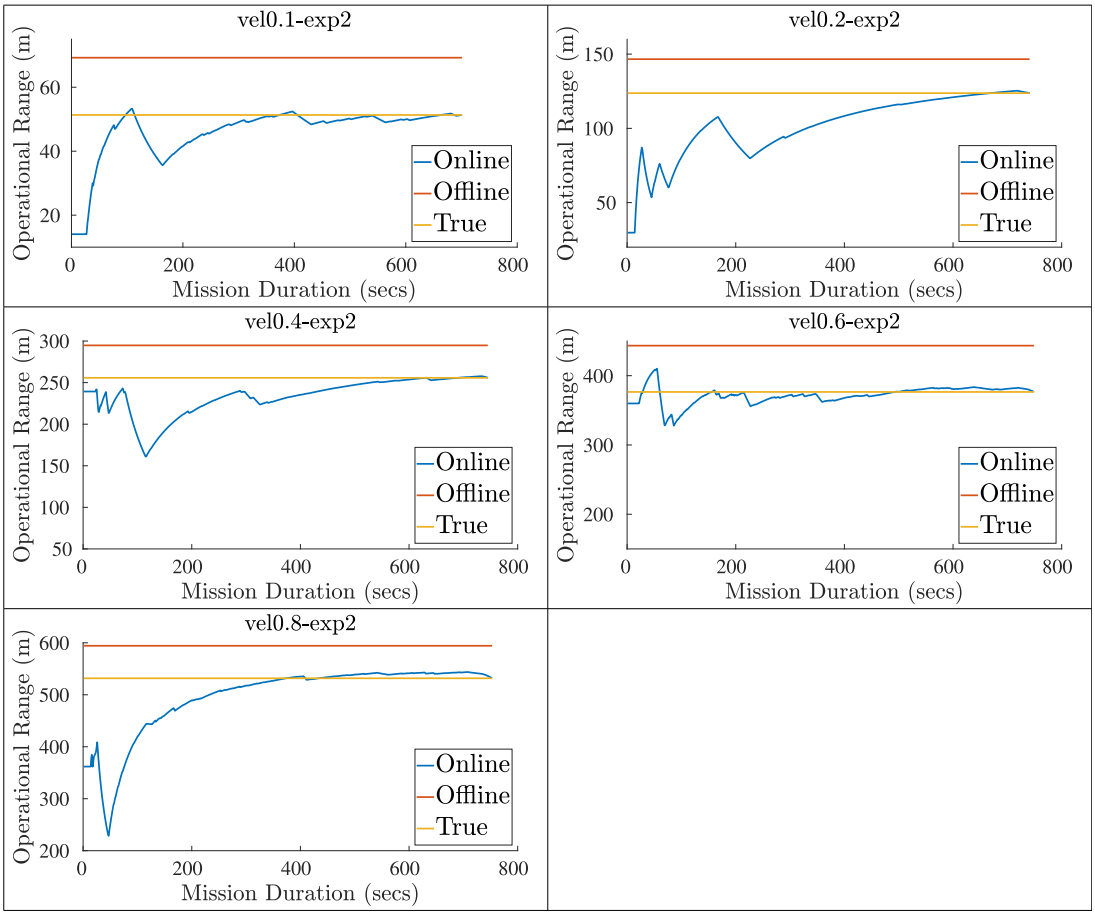

Fig. 12. Ardrone's operational range estimation at various velocities. The notation convention used in the figure labels are as follows: $vel*$ refers to the operational velocity used for the trial and exp^* refers to the experiment ID. In this figure, we have only shown the results obtained during experiment 2 for operational velocities in {0.1, 0.2, 0.4, 0.6} and {0.8}*m/sec* respectively.

operational velocity (v) always leads to an increase in the operational range (d). However, when the Ardrone attains an operational velocity v_{Opt} which is high enough, so much so, that the aerodynamic drag forces acting on the body of the drone is higher than that on the propeller, the theoretical maximum operational range (d_{Max}) will be attained and any further increase in the velocity will result in decrease in the operational range. Besides, such high velocities (v_{Opt}) are not attainable by current multi-rotor UAVs.

We would also like to highlight that the variance in the input data (wind compensation angle) being very low, results in low variance in $k(t)_{Env}$. This low variance in $k(t)_{Env}$, coupled with its low absolute value (1% on average), results in very low variance in predicted distance, often less than a meter. So for the sake of clear understanding of the experimental graphs, we have omitted the variance in predicted distance. From the data acquired from the field experiments, we see that the variance in wind compensation angle (θ) is very small. So using the information from Fig. 7, we see that the variance in $k(t)_{Env}$ will also be small. The variance in predicted operation range (Eq. (34)) will come from the factor $1 + k(t)_{Env}$. However, very small absolute value of $k(t)_{Env}$ (almost equal to 0.01) along with small variance leads to very small variance in $1 + k(t)_{Env}$, leading to small variance in predicted distance. This makes sense considering the fact that UAV experiments lasted for about 10 – 12 mins. and were carried out in calmer conditions for the safety of the drone. The variance in wind, and thus wind compensation angle would be small.

In Fig. 13, we showcase how the energy stored in the battery is consumed as the mission progresses. An interesting fact to note here is that the trends for both the *hovering* case and *motion* case are quite similar.

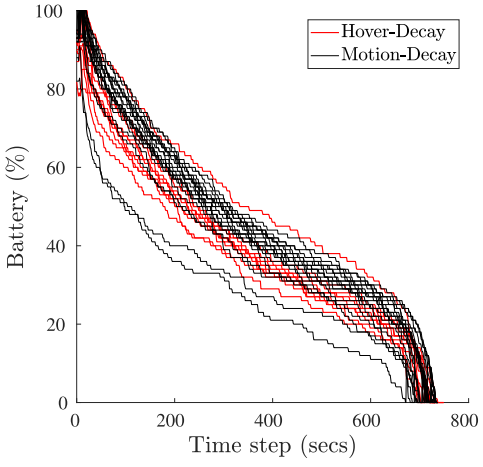

Fig. 13. Battery Decay for UAV while hovering and during motion.

The reason for this can be attributed to the fact that the value of $k(t)_{Env}$ which represents the average excess percentage of thrust that needs to be exerted to maintain stability and velocity, owing to changing environmental conditions, remains below 2%[10] So, the major component of

[10] Analyzed from the data obtained from *motion* experiments at varying velocities as shown in Fig. 12.

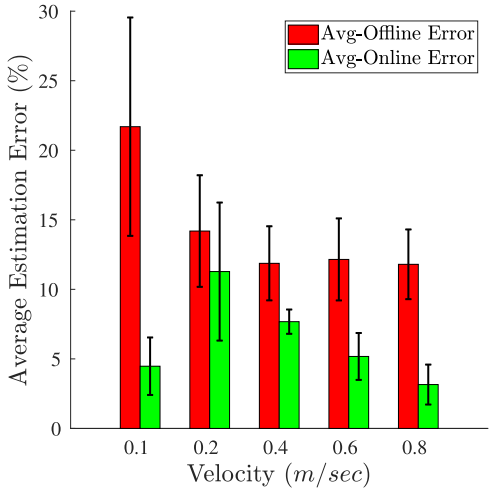

Fig. 14. Range estimation error. Plot showing error in operational range calculated using the *offline* and *online* models along with corresponding standard deviation.

energy is utilized to maintain flight (altitude) instead of stabilizing the rotorcraft and maintaining its velocity.

Fig. 14 shows the operational range estimation performance for both our proposed *online* and *offline* frameworks. For this, we report average estimation error of both frameworks for each operational velocity. It can be clearly seen from the graph that the *online* model is $\approx$58% more efficient than its counterpart. Also, to clarify the high *offline* estimation error at $v = 0.1\ m/s$, we would like to point out that even for small amounts of *hovering* time, the percentage difference in the average velocity and operational velocity is considerably higher than in cases of higher velocities which translates to higher percentage error in prediction using the *offline* model.

5. Conclusion

In this work, we have presented a methodology for identifying and quantifying the energy consumers for mobile robots. This work is an extension of our prior findings with the purpose of making our operational range estimation framework well suited to multiple robot platforms operating in real-world scenarios. The aim of this study was to unify the battery dissemination models into one framework that can now estimate operational range for various robotic platforms operating under realistic environmental conditions. Existing works focus on a pre-meditated mission profile and thereby try to estimate the energy requirements for the mission. However, the missions are usually limited by the available resources (energy stored in battery). Thus, we intend to solve the inverse problem of optimizing the mission profile given a fixed energy budget (governed by the battery type) and known robot dynamics model. The advantage of our framework is that it can be used for commercial and custom-built robots alike and is easily extendable to a plethora of platforms. Our framework is assisted by two operational range estimation models: *Firstly,* an *offline* model which relies on the expertise of the operator for setting the prior information, and, *secondly,* a self-reliant *online* variant that iteratively updates the operational range based on the available mission data. The advantage of proposing both variants in a unified framework could be realized from the fact that while the *offline* model allows the supervisor to set a rough upper bound on the path length of the robot at the beginning of the mission, the *online* model can recursively update the bound based on real-time performance data. High accuracy of our proposed framework ensures that the robots would return to base station thereby preventing them from getting stranded in the field during the mission.

Upon empirical evaluation, we verified that the framework incurs significantly lower error as compared to our prior work, and furthermore, the *online* model outperforms the *offline* variant. The *online* model estimates operational range with an average accuracy of 93.87%, while the *offline* model attains 82.97%. In light of this claim, our framework is well suited to be considered as a state-of-the-art for operational range estimation of a variety of robots operating under natural outdoor environmental conditions. In our further works, we would like to enhance our *ancillary functions*' energy consumption model by implementing SLAM [31] and mounting an array of additional sensors endowing our robot a full autonomy suit to make self-reliant decisions. In doing so, the energy consumed by the ancillary branch would significantly increase and thus, the importance of accurately estimating operational range from the residual maneuvering energy would become even more pronounced.

Acknowledgements

This work was supported by the Industrial Convergence Core Technology Development Program (No. 10063172) funded by MOTIE, Korea. We would like to thank Dr. A.A.R. Newaz, Boyu Tseng and Omran Hindawi for assisting with the experiments.

References

[1] Abdilla A, Richards A, Burrow S. Endurance optimisation of battery-powered rotorcraft. In: Conference Towards Autonomous Robotic Systems. Springer; 2015. p. 1–12.
[2] Abdilla A, Richards A, Burrow S. Power and endurance modelling of battery-powered rotorcraft. In: 2015 IEEE/RSJ International Conference on Intelligent Robots and Systems (IROS); 2015. p. 675–80. doi:10.1109/IROS.2015.7353445.
[3] Adams M, Halliop W. Aluminum energy semi-fuel cell systems for underwater applications: the state of the art and the way ahead. In: OCEANS'02 MTS/IEEE, 1. IEEE; 2002. p. 199–202.
[4] Aleksandrov D, Penkov I. Energy consumption of mini uav helicopters with different number of rotors. In: 11th International Symposium" Topical Problems in the Field of Electrical and Power Engineering; 2012. p. 259–62.
[5] Bekker M. Theory of land locomotion: the mechanics of vehicle mobility. Ann Arbor, MI:: University of Michigan Press; 2016.
[6] Bellingham JG, Rajan K. Robotics in remote and hostile environments. Science 2007;318(5853):1098–102.
[7] Berenz V, Tanaka F, Suzuki K. Autonomous battery management for mobile robots based on risk and gain assessment. Artif Intell Rev 2012;37(3):217–37.
[8] Bingham C, Walsh C, Carroll S. Impact of driving characteristics on electric vehicle energy consumption and range. IET Intel Transport Syst 2012;6(1):29–35.
[9] Broderick JA, Tilbury DM, Atkins EM. Characterizing energy usage of a commercially available ground robot: method and results. J Field Rob 2014;31(3):441–54.
[10] Economou J, Kladis G, Tsourdos A, White B. Uav optimum energy assignment using dijkstra's algorithm. In: Control Conference (ECC), 2007 European. IEEE; 2007. p. 287–92.
[11] Empatica. Real-time physiological signals-E4 EDA/GSR sensor. https://www.empatica.com/e4-wristband.
[12] Gatti M, Giulietti F, Turci M. Maximum endurance for battery-powered rotary-wing aircraft. Aerosp Sci Technol 2015;45:174–9.
[13] Graupe D., Beex A.A., Causey G.D.. Arma filter and method for designing the same. 1980. US Patent 4,188,667.
[14] Harrington AM, Kroninger C. Characterization of small dc brushed and brushless motors. Tech. Rep.. Army research lab aberdeen proving ground MD vehicle technology directorate; 2013.
[15] Hayes JG, de Oliveira RPR, Vaughan S, Egan MG. Simplified electric vehicle power train models and range estimation. In: Vehicle Power and Propulsion Conference (VPPC), 2011 IEEE. IEEE; 2011. p. 1–5.
[16] Kim H, Kim BK. Online minimum-energy trajectory planning and control on a straight-line path for three-wheeled omnidirectional mobile robots. IEEE Trans Ind Electron 2014;61(9):4771–9.
[17] Kim SW, Lee YH. Combined rate and power adaptation in ds/cdma communications over nakagami fading channels. IEEE Trans Commun 2000;48(1):162–8.
[18] Kwon E-M, Yu K-H, Yoon M-J, Jeong G-Y. Design considerations and modeling of a small and low altitude solar powered uav. In: Control, Automation and Systems (ICCAS), 2011 11th International Conference on. IEEE; 2011. p. 1085–8.
[19] Liu L, Shell DA. Large-scale multi-robot task allocation via dynamic partitioning and distribution. Auton Robots 2012;33(3):291–307.
[20] Liu S, Sun D. Minimizing energy consumption of wheeled mobile robots via optimal motion planning. IEEE/ASME Trans Mechatron 2014;19(2):401–11.
[21] Manley JE. Unmanned surface vehicles, 15 years of development. In: OCEANS 2008. IEEE; 2008. p. 1–4.
[22] Mei Y, Lu Y-H, Hu YC, Lee CG. Energy-efficient motion planning for mobile robots. In: Robotics and Automation, 2004. Proceedings. ICRA'04. 2004 IEEE International Conference on, 5. IEEE; 2004. p. 4344–9.

[23] Mei Y, Lu Y-H, Hu YC, Lee CG. A case study of mobile robot's energy consumption and conservation techniques. In: Advanced Robotics, 2005. ICAR'05. Proceedings., 12th International Conference on. IEEE; 2005. p. 492–7.
[24] Miller TF, Walter JL, Kiely DH. A next-generation auv energy system based on aluminum-seawater combustion. In: Autonomous Underwater Vehicles, 2002. Proceedings of the 2002 Workshop on. IEEE; 2002. p. 111–19.
[25] Murphy Robin R. Introduction to AI robotics. MIT press; 2000.
[26] Phillips A, Haroutunian M, Murphy AJ, Boyd S, Blake J, Griffiths G. Understanding the power requirements of autonomous underwater systems, part I: an analytical model for optimum swimming speeds and cost of transport. Ocean Eng 2015.
[27] Raugel E, Rigaud V, Lakeman C. Sea experiment of a survey auv powered by a fuel cell system. In: Autonomous Underwater Vehicles (AUV), 2010 IEEE/OES. IEEE; 2010. p. 1–3.
[28] Sadrpour A, Jin J, Ulsoy AG. Mission energy prediction for unmanned ground vehicles. In: Proc. of The IEEE International Conference on Robotics and Automation (ICRA). IEEE; 2012. p. 2229–34.
[29] Sadrpour A, Jin JJ, Ulsoy AG. Mission energy prediction for unmanned ground vehicles using real-time measurements and prior knowledge. J Field Rob 2013;30(3):399–414.
[30] Sato H. Moving average filter. 2001. US Patent 6,304,133.
[31] Thrun S, Leonard JJ. Simultaneous localization and mapping. In: Springer handbook of robotics. Springer; 2008. p. 871–89.
[32] Tiwari K, Xiao X, Chong NY. Estimating achievable range of ground robots operating on single battery discharge for operational efficacy amelioration. In: 2018 IEEE/RSJ International Conference on Intelligent Robots and Systems. IEEE; 2018. p. 3991–8.
[33] Toh TT, Mitcheson PD, Dussud L, Wright SW, Holmes AS. Electronic resonant frequency tuning of a marine energy harvester. Proceedings of the PowerMEMS, Seoul, Korea 2011;1518:383386.
[34] Traub LW. Range and endurance estimates for battery-powered aircraft. J Aircr 2011;48(2):703–7.
[35] Vergnano A, Thorstensson C, Lennartson B, Falkman P, Pellicciari M, Yuan C, et al. Embedding detailed robot energy optimization into high-level scheduling. In: Automation Science and Engineering (CASE), 2010 IEEE Conference on. IEEE; 2010. p. 386–92.
[36] Webb DC, Simonetti PJ, Jones CP. Slocum: an underwater glider propelled by environmental energy. IEEE J Oceanic Eng 2001;26(4):447–52.
[37] Yazici A, Kirlik G, Parlaktuna O, Sipahioglu A. A dynamic path planning approach for multi-robot sensor-based coverage considering energy constraints. In: Intelligent Robots and Systems, 2009. IROS 2009. IEEE/RSJ International Conference on. IEEE; 2009. p. 5930–5.

Kshitij Tiwari is a Postdoctoral Researcher at the Department of EEEA, School of Electrical Engineering, Aalto University, Finland. At the time of submission, he was a Ph.D. candidate at the Japan Advanced Institute of Science & Technology (JAIST), Japan. He obtained a M.Sc. in Artificial Intelligence with a special focus in Intelligent Robotics from the University of Edinburgh (2014) and a B.Engg. in Electronics & Communication from the University of Hong Kong (2013). His research interests include (but are not limited to) field robotics, applied Machine Learning, Neuronavigation, Path planning under uncertainty and related domains.

Xuesu Xiao is a Ph.D. student in the Department of Computer Science and Engineering at Texas A&M University, College Station, TX. He received his Master of Science degree in Mechanical Engineering in 2015 from Carnegie Mellon University, Pittsburgh, PA, Bachelor of Engineering dual-degree in Mechatronics Engineering in 2013 from Tongji University, China and FH Aachen University of Applied Sciences, Germany. His research interest focuses on robotic locomotion and motion planning.

Ashish Malik has completed his Bachelor of Engineering degree in Mechanical engineering in 2018 from Punjab Engineering College, India. At the time of this work, he was a research intern at Japan Advanced Institute of Science and Technology (JAIST) under the guidance of professor Nak Young Chong. His research interest include (but not limited to) field robotics and applied Machine Learning.

Nak Young Chong received the B.S., M.S., and Ph.D. degrees in mechanical engineering from Hanyang University, Seoul, Korea, in 1987, 1989, and 1994, respectively. From 1994 to 2007, he was a member of research staff at Daewoo Heavy Industries and KIST in Korea, and MEL and AIST in Japan. In 2003, he joined the faculty of Japan Advanced Institute of Science and Technology (JAIST), where he currently is a Professor of Information Science. He also served as a Councillor of JAIST and Director of the Center for Intelligent Robotics. He was a Visiting Scholar at Northwestern University, Georgia Institute of Technology, University of Genoa, and Carnegie Mellon University, and also served as an Associate Graduate Faculty at the University of Nevada, Las Vegas, and International Scholar at Kyung Hee University. He serves as Senior Editor of the IEEE Robotics and Automation Letters, Topic Editor-in-Chief of International Journal of Advanced Robotic Systems (Sage Publishing), and Journal of Intelligent Service Robotics (Springer), and served as Senior Editor of IEEE ICRA, IEEE CASE, IEEE Ro-Man, and UR 2018, and Associate Editor of the IEEE Transactions on Robotics. He served as Program Chair/Co-Chair for JCK Robotics 2009, ICAM 2010, IEEE Ro-Man 2011/2013, IEEE CASE 2012, URAI 2013/2014, DARS 2014, and ICCAS 2016. He was a General Co-Chair of URAI 2017. He also served as Co-Chair for IEEE-RAS Networked Robots Technical Committee from 2004 to 2006, and Fujitsu Scientific System Working Group from 2004 to 2008.